Energy Advances

Accepted Manuscript

This article can be cited before page numbers have been issued, to do this please use: R. Chen, V. Moradi, L. Hadidi and B. D. Gates, *Energy Adv.*, 2026, DOI: 10.1039/D5YA00314H.

ROYAL SOCIETY OF CHEMISTRY

rsc.li/energy-advances

View Article Online
DOI: 10.1039/D5YA00314H

One-Pot Synthesis for Doping and Coating NMC 811 with B, Al, and Nb for Enhanced Stability

*Rex Chen[1], Vahid Moradi[2], Lida Hadidi[2], and Byron D. Gates[1] **

[1]Department of Chemistry, Simon Fraser University, 8888 University Drive, Burnaby, BC V5A 1S6 (Canada)

[2] Nano One Materials Corporation, 8575 Government St., Burnaby, BC, V3N 4V1 (Canada)

* Corresponding Author: bgates@sfu.ca

View Article Online
DOI: 10.1039/D5YA00314H

Abstract

A promising cathode material is NMC 811 ($LiNi_{0.8}Mn_{0.1}Co_{0.1}O_2$), but its commercial adoption is hindered by structural and surface degradation, which cause rapid capacity fading. This degradation manifests as cation mixing, microcrack formation, parasitic side reactions arising from HF attack and oxygen release, collectively compromising the material's long-term stability. To address this, we investigated a multi-element strategy using a patented one-pot Metal-to-Cathode Active Material (M2CAM®) process to simultaneously dope and coat the material with boron, aluminum, and niobium. This approach is designed to synergistically enhance the cathode's stability. Comprehensive material analysis and electrochemical testing (galvanostatic cycling and rate capability) were performed. The results show that NMC 811 doped with B, Al, and Nb achieved a capacity retention of ~91% after 100 cycles at 1C, a significant improvement over the ~76% retention exhibited by the pristine material. This enhancement is attributed to both bulk structural stabilization by the dopants and improved surface integrity provided by a concurrently formed niobium-based coating. This scalable, single-step synthesis offers a viable path to producing durable, high-performance cathodes for demanding applications, such as electric vehicles and grid-scale storage. These findings highlight the effectiveness of multi-component, single-step modifications in overcoming the intrinsic limitations of Ni-rich cathode materials.

Keywords: Lithium-ion batteries, Ni-rich cathode, doping, coating, synthesis

View Article Online
DOI: 10.1039/D5YA00314H

Introduction

This paper investigates modifications to NMC 811 ($LiNi_{0.8}Mn_{0.1}Co_{0.1}O_2$) cathode materials through multi-elemental doping and coating using boron, aluminum, and/or niobium to mitigate cathode degradation during battery operation. Incorporation of these species is sought to address critical challenges that undermine the structural integrity and electrochemical performance of high-nickel NMC[1]. As the global transition to clean energy accelerates, lithium-ion batteries (LIBs) continue to play a pivotal role in enabling technologies ranging from electric vehicles (EVs) to large-scale renewable energy storage systems[2]. Within LIBs, the cathode is a crucial component, as it largely determines the battery's energy density, operating voltage, and overall performance[3,4]. The demand for higher energy density, longer lifespans, and improved safety in LIBs continues to drive further research into the preparation of advanced cathode materials[5,6]. Among the many cathode materials available, nickel-rich layered oxides, such as NMC 811, stand out due to their high specific capacity, superior energy density[7], and reduced reliance on cobalt, which is a scarce and ethically contentious resource[8,9]. Compared to other cathode materials, nickel-rich cathodes offer a compelling balance of high capacity and cost efficiency[10,11]. For example, NMC 811 offers a high specific capacity, typically around 200 to 220 mAh/g, surpassing other NMC compositions, such as NMC 111 (Ni:Mn:Co = 1:1:1) that is typically around 150 mAh/g[12]. This high specific capacity translates into a higher energy density, making NMC 811 particularly suitable for applications requiring long runtimes, such as for EVs[13]. In fact, NMC 811 provides one of the highest energy densities in the NMC family, ranging from 200 to 250 Wh/kg[14]. These attributes make NMC 811 a leading potential cathode material for next-generation LIBs.

Despite these advantages, NMC 811 is limited by poor long-term stability, stemming from a combination of interconnected degradation mechanisms. The high nickel content in NMC 811

View Article Online
DOI: 10.1039/D5YA00314H

introduces challenges such as cation mixing. Cation mixing occurs when nickel ions migrate and replace lithium ions in the lattice—due to their similar ionic radii—during battery operation and/or during the synthesis of the cathode material, leading to structural instability, decreased performance, and a shortened lifespan[15]. Moreover, the significant anisotropic volume changes during repeated cycling induce internal stress, leading to the formation of microcracks within the secondary particles[16]. These cracks expose new, reactive surfaces to the electrolyte, thereby accelerating parasitic side reactions[17]. Such side reactions include hydrofluoric acid (HF) attack, where HF, formed from the reaction of trace moisture with $LiPF_6$ in the electrolyte, leads to the dissolution of transition metals[18]. Furthermore, at high states of charge, the delithiated structure becomes unstable, triggering the release of oxygen from the lattice. This process not only promotes an irreversible phase transition from the layered structure to the spinel and rock-salt phases, but also creates a significant safety risk, as the released oxygen can react exothermically with the flammable organic components of the electrolyte and can initiate a thermal runaway[19]. Collectively, these degradation pathways result in rapid capacity fading, lower power output, and risk of battery fires.

To address the challenges of cathode degradation associated with NMC 811, researchers have turned to two complementary materials engineering strategies: (i) doping; and/or (ii) coating of cathode particles[20-21]. Doping entails the intentional substitution of foreign cations or anions into the bulk lattice of NMC materials. This structural modification can adjust the local charge distribution, influence lattice constants, and suppress cation mixing[22,23]. Larger or more electropositive dopants such as Al^{3+} or Zr^{4+} can increase the lattice spacing, reducing structural re-arrangement of the Ni^{2+} and Li^{+} sites, and improve the thermodynamic stability of the structure[24,25]. Additionally, certain dopants can introduce stronger metal-oxygen bonds, which decrease oxygen

View Article Online
DOI: 10.1039/D5YA00314H

release from the lattice and delay surface reconstruction processes[26]. These changes result in enhanced structural resilience, reduced voltage fade, and suppressed microcrack formation, especially under high-voltage operation. By relieving internal lattice strain and minimizing anisotropic volume changes during delithiation/lithiation processes, doping also helps prevent intragranular and intergranular cracking, which are common degradation pathways for Ni-rich layered oxides[27]. Moreover, doping can reduce the formation of anti-site (or place-exchange) defects and can facilitate more reversible Li^+ transport pathways, thereby improving rate capability and long-term cyclability[28].

Surface coating techniques can be used to modify the interface between the NMC particles and the liquid electrolyte. Thin layers of protective materials are deposited onto the surfaces of particles to inhibit direct contact with the electrolyte, thus reducing reactions that lead to surface degradation[29,30,31]. Coating materials may include inert oxides (e.g., Al_2O_3, ZrO_2)[32,33], lithium-conductive ceramics (e.g., $Li_4Ti_5O_{12}$)[34,35], phosphates (e.g., Li_3PO_4)[36], fluorides[37], and even borate-based compounds[38,39,40]. These coatings serve multiple roles: (i) as physical barriers that prevent potential HF attack and transition metal leaching; (ii) as chemical buffers that neutralize acidic electrolyte components; and (iii) as electrochemical stabilizers that mitigate electrolyte decomposition at high potentials[41,42]. In lithium-containing coatings, the layer can also participate in lithium-ion conduction, maintaining interfacial conductivity while providing these protective properties[43]. Importantly, coatings can also help mitigate surface-induced mechanical degradation. By minimizing interfacial side reactions and stabilizing surface structures, coatings reduce the buildup of internal stress gradients and suppress the propagation of surface cracks into the bulk[44]. Advanced coating methods such as atomic layer deposition (ALD)[45], sol-gel synthesis[46], and ball milling followed by thermal treatment[47,48] are increasingly used by researchers to achieve uniform

View Article Online
DOI: 10.1039/D5YA00314H

and conformal coverage. While single dopants and coatings may enhance specific aspects of NMC stability, the approach often falls short of fully mitigating structural and electrochemical challenges under diverse operating conditions. Notably, limited studies have explored the implementation of multiple dopants to achieve a synergistic effect.

Boron doping is of interest for its ability to strengthen the crystal lattice, create strong boron-oxygen bonds, and mitigate transition metal migration[49,50,51]. Previous studies reported that boron incorporation into the NMC structure can improve cycling performance by stabilizing the layered structure and suppressing undesired phase transitions. Co-doping of NMC with multiple elements, such as aluminum and niobium, is effective in reducing the lattice strain and minimizing mechanical degradation[52,53]. These properties of Al and Nb may be complementary to the effects of B. The study presented herein aims to utilize a new, commercial, one-pot synthetic process to create boron-, aluminum-, and/or niobium- co-doped NMC 811 particles with a multi-element coating, thereby simultaneously addressing challenges that include cation mixing, lattice strain, and surface degradation. By leveraging the complementary properties of elements such as boron, aluminum, and niobium, this study aims to investigate whether a multi-elemental doping and coating strategy can provide a more robust solution for stabilizing NMC 811 during battery operation.

This study systematically investigates the synergistic effects of multi-element doping and coating on the stability of NMC 811. A series of materials, including pristine NMC 811, B-NMC 811, B-Al-NMC 811, B-Nb-NMC 811, and B-Al-Nb-NMC 811, were synthesized using Nano One Materials Corp.'s patented, streamlined one-pot process known as Metal-to-Cathode Active Material (M2CAM®). To achieve a balance between structural reinforcement and minimal disruption to the primary NMC lattice, the dopant levels were controlled at 1 mol% boron (~0.1

View Article Online
DOI: 10.1039/D5YA00314H

wt%), 1 mol% aluminum (~0.3 wt%), and 0.5 mol% niobium (~0.5 wt%) relative to 1 mol of total transition metals. These concentrations are intended to enhance stability without significantly altering the material's bulk electrochemical properties. This method directly converts raw metal powders and dopant precursors into the final cathode active material, offering a scalable and efficient pathway for producing advanced cathode materials. The resulting powders were comprehensively characterized to understand the correlation between composition, structure, and performance. Material analysis techniques, including X-ray diffraction (XRD), scanning electron microscopy (SEM), and transmission electron microscopy (TEM) coupled with energy-dispersive X-ray spectroscopy (EDS), were employed to examine the bulk structure, particle morphology, and elemental distribution. X-ray photoelectron spectroscopy (XPS) was used to investigate the surface chemistry and identify the species in the coatings on the NMC particles. Finally, the electrochemical performance of each material was evaluated through galvanostatic cycling, rate capability tests, and differential capacity analysis to correlate the modifications with improvements in cycle life and stability.

Experimental Methods

Synthesis of Modified NMC 811 Cathode Materials

The methodology begins with the synthesis of all cathode materials, including the baseline pristine NMC 811, using Nano One Material Corp.'s M2CAM® technology, in which transition metals are directly added to a one-pot solution to be transformed into cathode active material[54,55]. The authors were granted explicit permission to utilize this process. This study modifies this process to incorporate co-doping or co-coating of boron-based precursors alongside aluminum and niobium species. Elemental nickel, manganese, and cobalt were combined with stoichiometric amounts of boron, aluminum, and niobium precursors in a single reaction vessel. The boron

View Article Online
DOI: 10.1039/D5YA00314H

precursor used was boric acid (H_3BO_3), while aluminum and niobium were introduced using proprietary precursors. The concentration of each dopant was ~0.11, 0.27, and 0.46 wt% of boron, aluminum, and niobium, respectively. The mixture was continuously stirred throughout the reaction to facilitate the formation of a homogeneous solution. After completing the reaction, the product was spray-dried to obtain the precursor cathode active material (pCAM). This pCAM was subjected to thermal processing in a tube furnace under an oxygen atmosphere to obtain the cathode active material (CAM). The materials were heated from ambient temperature to 800 °C at a rate of 5 °C/min, held at 800 °C for 10 h, and cooled passively to the ambient temperature. The resulting powder was subsequently ground with an agate mortar and pestle into a fine powder for characterization and electrochemical testing. The baseline pristine NMC 811 was prepared under the same reaction conditions as the modified samples.

Compositional and Structural Characterization

This study characterized bulk properties using compositional and structural analysis techniques. Inductively coupled plasma – optical emission spectroscopy (ICP-OES) was used to measure the elemental composition, calculate the elemental ratios of dopants relative to the transition metals, and verify alignment with the intended stoichiometry, confirming the incorporation of boron, aluminum, and niobium. This study weighed 0.8 g of pCAM and 0.4 g of CAM, then transferred each sample into a microwave digestion vessel. Then, 15 mL of concentrated hydrochloric acid and 5 mL of concentrated nitric acid were added to each vessel. *Caution: these acids are corrosive, and proper techniques should be used when handling these reagents.* The digestion process was performed using an Anton Paar Multiwave GO Plus Microwave Digester. The temperature of the sample was ramped to 170 °C over 10 min, held at this target temperature for 5 min, and cooled to 40 °C. Following digestion, this study used a

View Article Online
DOI: 10.1039/D5YA00314H

Microlab 600 Auto-diluter to dilute 200 µL of each sample with 9800 µL of a 2% HNO_3 solution containing 2 g/L KCl. An Agilent 5110 VDV ICP-OES was used to analyze the samples, using calibration standards containing Al, B, Co, Li, Mn, Nb, and Ni at various concentrations. Multiple emission wavelengths for the selected elements were examined to ensure accurate and reliable results.

X-ray diffraction (XRD) was utilized to determine the crystal structure and phase composition of pristine and modified NMC 811 samples. To prepare the powder samples, flat glass sample holders were packed with material and measured using a Rigaku MiniFlex 6G with Cu Kα radiation as the X-ray source. Diffraction data were collected over a 2θ range of 3° to 90° with a step size of 0.01°. Operating conditions included a tube voltage of 40 kV and a tube current of 15 mA to ensure high resolution for measuring peak positions, intensity ratios, and peak broadening. GSAS II was used to refine the XRD patterns and to extract lattice parameters. Calculations of the intensity ratio of the (003) and (104) peaks evaluated the extent of cation mixing in the powders. Changes in the a, b, and c lattice parameters assessed the impact of doping on the crystal structure. Peak broadening provided insights into the crystallinity of the pristine and doped samples.

Morphology, Additional Composition, and Surface-Based Analyses

The surface properties of the synthesized materials were evaluated to investigate the chemical composition, morphology, and uniformity of surface coatings or other modifications (i.e., doping). High-resolution transmission electron microscopy (HRTEM) and scanning transmission electron microscopy coupled with energy-dispersive X-ray spectroscopy (STEM-EDS) were used to examine the structural and compositional characteristics of pristine and doped NMC 811 samples. These techniques were also used to assess the uniformity and distribution of dopants between the “bulk” of the particles and their surfaces. The HRTEM and STEM-EDS imaging was

View Article Online
DOI: 10.1039/D5YA00314H

performed using an FEI Tecnai Osiris S/TEM at an accelerating voltage of 200 kV to analyze the structural and compositional characteristics of the particles. Preparation for both methods involved dispersing a small quantity of powder in 1.0 mL of isopropanol (IPA), applying ultrasonication for ~30 s, and placing 25 μL of the suspension onto a lacey carbon-coated copper grid before drying under vacuum (~230 Torr) in a sealed desiccator for >1 h.

The surface properties of the synthesized material were evaluated to investigate the chemical composition, morphology, and uniformity of surface coatings or modifications. HRTEM analysis focused on lattice fringes, surface features, and the presence of amorphous coatings, with images analyzed using Digital Micrograph (DM). STEM-EDS techniques were used to map the elemental distributions of key components within the particles, including Ni, Mn, Co, Al, Nb, and lighter elements such as boron and carbon. Due to its very light atomic weight, boron is challenging to detect accurately with EDS. Potential spectral overlap with carbon requires careful interpretation, particularly when carbon contamination may result from sample preparation and handling. Elemental segregation between the bulk and surface regions of the modified NMC 811 samples was investigated, with specific attention given to the possible formation of a coating. To enhance imaging and analytical accuracy, HRTEM and STEM-EDS samples were plasma-cleaned using a Fischione Model 1020 Plasma Cleaner. This step is essential to remove carbonaceous contamination that can degrade image contrast and obscure fine structural details when samples are exposed to the electron beam. A gentle plasma composed of 25% oxygen and 75% argon was used under vacuum conditions. The TEM holders were placed in the plasma chamber and exposed to plasma for 15 s to clean the surfaces of the samples.

Scanning electron microscopy (SEM) techniques were used to analyze the morphology of pristine and modified NMC 811 particles. Preparation involved dispersing a small quantity of

View Article Online
DOI: 10.1039/D5YA00314H

powder in 1.0 mL of IPA, followed by ultrasonication treatment for ~30 s, and depositing a 50 μL droplet of the suspension onto a silicon wafer affixed to an aluminum SEM sample stub with carbon tape. The samples were subsequently dried under vacuum. The SEM imaging was performed using a Thermo Scientific Quattro S ESEM equipped with a secondary electron detector to capture surface morphology. The accelerating voltage was set to 20 kV with a 3-nm diameter spot size to optimize resolution while minimizing charging effects. The working distance was adjusted to 10 mm, which was found to be sufficient for obtaining high-quality SEM images of the required resolution and contrast. The particles were imaged at magnifications ranging from 1,000× to 250,000× to observe their size, shape, and distributions therein.

X-ray photoelectron spectroscopy (XPS) was used to determine the surface elemental composition and oxidation states, with a focus on the presence and potential distribution of the boron, aluminum, and/or niobium species. Sample preparation and measurements were conducted using a Kratos Ultra XPS system at the nanoFAB at the University of Alberta.

Electrochemical Performance Evaluation

Electrochemical analyses for half-cells made from the pristine and modified NMC 811 materials were performed using CR2032 coin cells. Cathode slurries of the NMC 811 powders were prepared by mixing them with conductive carbon black (C65, Gelon LIB Group) and polyvinylidene fluoride (PVDF, Solvay, Solef 51300/1001 high viscosity grade) binding solution in N-methyl-2-pyrrolidinone (NMP, Gelon LIB Group, electronic grade 99.9%) solvent. The final weight ratio of the solid contents was 90% NMC 811 cathode material, 7% carbon black, and 3% PVDF. The resulting ink was cast on a 16 μm-thick graphite-coated aluminum foil current collector using a doctor blade to form a thin electrode with an NMC weight loading of 5 mg/cm^2. The

View Article Online
DOI: 10.1039/D5YA00314H

electrodes were dried for 24 h at 80 °C under vacuum (≥ 685 Torr). The electrodes were then calendared to a thickness of ~35 μm to achieve an approximate electrode density of 3 g/cm^3.

A series of 1.5 cm^2 disks were cut from the electrodes and transferred into an argon-filled glovebox to be assembled into the coin cells. Lithium foil disks, 340-μm in thickness, were used as counter and reference electrodes. The electrolyte used was a 1 M $LiPF_6$ solution in an ethylene carbonate (EC), ethyl methyl carbonate (EMC), and dimethyl carbonate (DMC) mixture plus 1% vinylene carbonate (VC) electrolyte additive. The polypropylene separators in the coin cells were 19 mm in diameter and 25 μm in thickness. An electric crimper was used to assemble and seal the cells. Six replicate cells were prepared for each of the five materials, totaling 30 cells. The assembled cells were removed from the glovebox and allowed to rest for more than 16 h before initiating the electrochemical tests. The cells were conditioned for one cycle at a rate of C/20 and two cycles at C/10. In each set of samples, three cells were taken for cycling and the other three for rate capability tests. Cells were cycled at a rate of 1C over the voltage range from 2.8 V to 4.3 V (vs Li/Li$^+$) for 100 cycles at 25 °C. During the 1C cycling, an additional potentiostatic charge step at 4.3 V was applied to the cells for 10 min. Rate capability was assessed by cycling the cells at rates of 0.1C, 0.5C, 1C, 3C, 5C, and 10C, followed by a return to 0.1C at 25 °C to evaluate capacity recovery. Differential capacity measurements were conducted simultaneously and automatically during cycling.

View Article Online
DOI: 10.1039/D5YA00314H

Results and Discussion

Inductively coupled plasma–optical emission spectroscopy (ICP-OES) was used to determine the elemental composition, calculate elemental ratios relative to transition metals, and verify consistency with the target stoichiometry. While these results confirm the presence of boron, aluminum, and niobium in the materials before calcination (**Table S1**) and the cathode active material after calcination (**Table S2**), the specific structural incorporation of these elements into the structure of the final cathode active material is established through the subsequent crystallographic and surface analyses.

Particle Morphology and Structure

Figure 1 presents typical SEM images of the pristine and modified NMC 811 samples at different magnifications, illustrating the impact of boron, aluminum, and niobium on primary particle size and morphology. Images obtained at a lower magnification (**Figure 1a to 1e**) show spherical secondary particles for both the pristine and modified NMC 811 materials. Focusing on the primary particles, the pristine NMC 811 exhibits relatively smooth, rounded primary particles (**Figure 1k**). This morphology is characteristic of conventionally synthesized NMC materials, where controlled grain growth results in a polycrystalline structure with faceted yet continuous surfaces[60,61,58]. The absence of a significant surface roughness suggests that minimal secondary phases or defects are present.

Upon doping NMC with 1 mol% boron (~0.11 wt%), referred to as B-NMC 811, a notable transformation in primary particle morphology is observed (**Figure 1l**). The primary particles become smaller and adopt a blockier, more angular structure compared to the pristine material. This shift indicates that boron may interfere with grain growth kinetics during high-temperature treatment. Boron may induce preferential growth towards certain crystal planes due to the change

View Article Online
DOI: 10.1039/D5YA00314H

in primary particle shape[59]. The formation of sharper edges could introduce structural weaknesses, making the particle more susceptible to cracking and electrolyte reactivity as the particle expands and contracts during cycling tests[60,61].

When aluminum is co-doped with boron, referred to as B-Al-NMC 811, the resulting morphology is similar to that of the B-NMC 811 sample (**Figure 1m**). The primary particles remain small and blocky, indicating that aluminum does not significantly counteract boron's inhibition of the grain growth in the NMC 811 particles. Aluminum is known to stabilize layered oxide structures by substituting transition metals, reducing cation disorder, and improving thermal stability. However, in this case, its presence does not appear to promote grain fusion or densification. Instead, the persistence of a blocky morphology suggests that aluminum does not significantly enhance sintering, leaving the boron-induced particle structure essentially unchanged.

Interestingly, the addition of niobium to the NMC 811 cathode material (referred to as B-Nb-NMC 811 or B-Al-Nb-NMC 811) results in noticeably rounder primary particles (**Figure 1n and 1o**) compared to B-Al-NMC 811 and B-NMC 811 due to its influence on particle growth kinetics. The Nb-doping appears to promote isotropic growth over anisotropic growth. This occurs because niobium incorporation likely decreases the differences in surface energies among various crystallographic planes, encouraging uniform and symmetrical particle growth rather than favoring specific directional growth[62,63]. As a result, primary particles appear smoother and more spherical. Furthermore, lattice distortions introduced by niobium enhance atomic mobility and mass transport during particle formation, allowing for a smoother redistribution of atoms across the particle's surfaces. This improved diffusion process results in a reduction in the presence of surface irregularities and promotes the development of smoother, rounder particle edges.

View Article Online
DOI: 10.1039/D5YA00314H

These observations demonstrate that boron can significantly influence particle morphology by inhibiting grain growth, resulting in smaller and blockier primary particles. The addition of aluminum does not significantly alter this effect for NMC 811. The presence of niobium does, however, appear to restore the original smooth, rounded primary particle shape (although the primary particle size is slightly decreased compared to the pristine material). The B-Al-Nb-doped sample exhibits a morphology similar to the pristine and B-Nb-doped materials, suggesting that aluminum and niobium can work synergistically to overcome the structural modifications introduced by boron. These morphological differences are expected to influence electrochemical performance, particularly in terms of lithium-ion diffusion, structural stability, and capacity retention. Analysis of the secondary particle size distribution complements the SEM observations (**Figure S1**, **Table S3**). In general, the doped samples show a modest reduction in the median particle size (referred to as D50) and a narrower overall size distribution. The B-Al-NMC 811 sample is a key exception, as it shows a larger median particle size than the pristine material, which suggests that aluminum may promote secondary particle agglomeration. Notably, the niobium-containing samples exhibit the smallest "D90 values", indicating that the addition of niobium species is particularly effective at controlling the upper limits of particle growth and producing a more homogeneous final product.

Analysis by XRD reveals substantial structural differences between the pristine and doped NMC 811 samples, including notable changes in peak intensity ratios, lattice parameters, and peak splitting patterns (**Figure 2**). Furthermore, a detailed analysis of the lattice parameters from Rietveld refinement provides quantitative evidence for these structural changes (**Table 1**, **Figure S2**). The low values for the weighted profile residuals (Rwp) from the refinement for each sample confirm a good fit between the experimental data and the calculated structural model. All major

View Article Online
DOI: 10.1039/D5YA00314H

diffraction peaks for the pristine and modified samples can be indexed to the α-$NaFeO_2$ layered structure with an $R\bar{3}m$ space group, which is characteristic of NMC 811. In pristine NMC 811, the intensity ratio of the (003) to (104) peaks (I_{003}/I_{104}) is 1.4326. The I_{003}/I_{104} ratio is a key crystallographic indicator of cation mixing. A high ratio, typically >1.2, signifies a low degree of cation mixing and thus a well-ordered layered structure, which is essential for facile Li^+ diffusion[64,65]. The observed value confirms a high degree of structural integrity in the pristine material. However, once the dopants are introduced into the NMC lattice, their I_{003}/I_{104} ratios decline, with B-NMC 811 having the lowest I_{003}/I_{104} value of 0.9911. This may indicate structural disruptions and increased cation mixing in the cathode powders. A similar trend has been previously reported, where excess boron concentration (5 at%) in NMC 811 resulted in a decreased I_{003}/I_{104} ratio of 1.12[50]. While the literature value of 5 at% is significantly higher than the 0.3 at% B used in this study (**Table S5**), our results show an even more pronounced decrease in the I_{003}/I_{104} ratio to 0.9911, suggesting that the NMC 811 is exceptionally sensitive to boron incorporation and that this sensitivity may depend on the synthesis method. This decrease could be attributed to a localized lithium deficiency caused by the reaction of boron with the lithium source during synthesis. The resulting vacancies in the lithium layers become energetically favorable sites for Ni^{2+} migration from the transition metal layers. The initial doping concentrations for this study were selected as a conservative starting point, aiming to leverage the potential stability benefits from doping while deliberately avoiding structural degradation reported at higher concentrations (e.g., 5 at% B). However, a significant increase in cation mixing was observed in the B-NMC 811 sample, indicating that even this low boron concentration was excessive.

The c/a ratio, which reflects the degree of hexagonal ordering in the layered structure, provides further insight into the structural stability of the materials. A higher c/a ratio indicates a

View Article Online
DOI: 10.1039/D5YA00314H

more distinct and well-ordered layered structure, which is desirable for efficient lithium-ion transport[66]. Conversely, a lower ratio often points to a more compressed and disordered structure, which is frequently associated with increased cation mixing. The pristine NMC 811 material exhibits a c/a ratio of 4.9440, serving as a baseline for comparison (**Table 1**). For B-NMC 811, a slight expansion in the a-axis (2.8726 Å) is coupled with a more significant contraction in the c-axis (14.1819 Å), leading to a reduced c/a ratio of 4.9370. Such a reduction in the c/a ratio is generally undesirable as it can negatively affect the electrochemical performance of the NMC cathode particles by promoting cation mixing and structural degradation during electrochemical cycling. In contrast, the co-doped samples show different trends. The addition of aluminum in B-Al-NMC 811 appears to counteract the c-axis contraction, increasing the c/a ratio to 4.9408. The B-Nb-NMC 811 and B-Al-Nb-NMC 811 samples exhibit the largest lattice volumes of the series, at 101.474 $Å^3$ and 101.488 $Å^3$, respectively. This expansion may be driven by an increase in the a-lattice parameter, particularly for the B-Al-Nb-NMC 811 sample (a = 2.8734 Å), suggesting that the combined incorporation of the dopants induces an expansion within the transition metal layers, which could influence Li^+ diffusion kinetics and structural stability during cycling.

Surface Chemistry and Elemental Distribution of Modified NMC 811

Analyses by STEM-EDS confirmed that the addition of 0.5 mol% (~0.46 wt%) Nb led to the successful creation of a thin, uniform niobium-rich coating layer on the surface of B-Nb-NMC 811 and B-Al-Nb-NMC 811 cathode particles after thermal treatment. Elemental mapping indicates Nb enrichment at the particle interface, demonstrating that niobium can still diffuse to the surface when other dopants are present (**Figure 3a and 3c**). It may be possible for boron to also diffuse to the surface. However, boron's atomic radius is small and produces a low yield of X-rays, which makes accurate detection of boron by STEM-EDS techniques challenging. The

View Article Online
DOI: 10.1039/D5YA00314H

thermal treatment was conducted under a flowing oxygen atmosphere, and these highly oxidizing conditions at elevated temperatures are known to promote the surface segregation of niobium in polycrystalline oxides[67]. This phenomenon occurs as niobium species migrate through lattice vacancies and grain boundaries, driven by concentration gradients and energy minimization processes[68], ultimately accumulating at the surface. The subsequent formation of a coating is expected to significantly mitigate cathode degradation during battery operation.

In addition to the dopant distribution, the spatial arrangement of the transition metals was investigated by STEM-EDS. The elemental maps for B-Nb-NMC 811 and B-Al-Nb-NMC 811 confirm a homogenous distribution of Ni, Mn, and Co throughout the primary particles (**Figure 3b and 3d**). Such uniformity is a critical attribute for high-performance cathode materials, as it ensures consistent structural properties and electrochemical activity across the particle volume. This homogeneity is expected to mitigate the formation of localized stress concentrations that can arise from anisotropic lattice changes during cycling, thereby suppressing a key mechanism for microcrack initiation. Furthermore, a uniform distribution of transition metals promotes consistent Li-ion diffusion pathways and electronic conductivity, which are essential for realizing a high-rate capability and long-term cycling stability. Since the pristine (**Figure S3**) and modified materials all exhibit this same degree of transition metal homogeneity, the significant differences in their electrochemical performance may not be attributed to the underlying distribution of Ni, Mn, and Co. This finding strongly suggests that the superior stability of the co-doped materials may be a direct consequence of the dopants and resulting surface coatings, highlighting the distinct and critical role these modifications play in enhancing the cathode's performance beyond its baseline structural properties.

View Article Online
DOI: 10.1039/D5YA00314H

An XPS analysis also confirmed the presence of niobium on the surface of both B-Nb-NMC 811 and B-Al-Nb-NMC 811 samples (**Figure 5**, **Figure S7**). All binding energies were calibrated to the adventitious carbon C 1s peak at 284.8 eV to correct for surface charging. Distinct Nb 3d peaks were observed at binding energies of 206.8 eV and 209.5 eV with a split of 2.7 eV, corresponding to the Nb $3d_{5/2}$ and Nb $3d_{3/2}$ orbitals, respectively[69]. These binding energies are consistent with niobium oxide species containing Nb^{5+}, such as Nb_2O_5[70], which is commonly associated with surface coatings rather than bulk substitution within the layered lattice. The relatively strong signal intensity of the Nb 3d peaks suggests that the niobium is enriched at the particle surface rather than being uniformly distributed throughout the particles. This surface localization implies that during thermal treatment, Nb precursors may have migrated toward the surface and reacted to form a thin, possibly amorphous Nb-based oxide. Such coatings are known to enhance interfacial stability by suppressing undesired surface reactions, such as electrolyte decomposition and transition metal dissolution, thereby improving the long-term electrochemical performance of the cathode[71]. The consistent detection of Nb on the surface of each of these multi-doped compositions of NMC 811 reinforces the hypothesis that Nb plays a key role in forming a protective layer at the particle–electrolyte interface.

To investigate the structural nature of the particle interfaces, HRTEM was performed on both the pristine and the B-Nb-NMC 811 sample (**Figure 4**). The HRTEM image of the pristine material reveals highly ordered crystalline lattice fringes extending directly to the outermost edges of the particle. In contrast, the B-Nb-NMC 811 sample exhibits a distinct amorphous layer at the particle boundary, highlighted by the red dashed lines. When correlated with the localized niobium enrichment observed in the STEM-EDS mapping (**Figure 3**) and the surface Nb5+ species

View Article Online
DOI: 10.1039/D5YA00314H

identified via XPS (**Figure 5**), this amorphous interphase may indicate the formation of a protective niobium-based coating.

To further evaluate the surface composition of the co-doped materials, high-resolution XPS of the Al 2p region was conducted on the B-Al-NMC 811 and B-Al-Nb-NMC 811 samples (**Figure S8**). In contrast to the distinct niobium signals, no discernible Al 2p peak was detected above the baseline noise. This absence of a measurable signal indicates that the surface concentration of aluminum is below the detection limit of the XPS instrument. Consequently, this suggests that unlike niobium, which readily migrates to the particle surface during thermal treatment, aluminum preferentially incorporates into the bulk lattice of the NMC 811 structure rather than forming a surface-segregated layer.

To investigate the chemical environment and surface localization of boron in the modified NMC 811 materials, additional high-resolution XPS analyses of the B 1s region were performed on four representative compositions: (i) B-NMC 811; (ii) B-Nb-NMC 811; (iii) B-Al-NMC 811; and (iv) B-Al-Nb-NMC 811 (**Figure 6**). Prolonged integration times were used to enhance the intensity of the boron signal, given the inherently low photoionization cross-section of B and the low B concentration (0.11 wt%) in these samples. All spectra exhibit a broad B 1s peak consistent with a B-O bond[50,72], confirming that boron is retained in the final material. However, the peak center varies slightly depending on the co-dopants: 190.7 eV for B-NMC 811; 191.1 eV for B-Al-NMC 811; 190.3 eV for B-Nb-NMC 811; and 190.6 eV for B-Al-Nb-NMC 811. These small shifts in binding energy may reflect changes in the local chemical environment of the boron atoms, likely influenced by the electronegativity of the neighboring dopants[73]. The higher binding energy in the B-Al-NMC 811 sample, for example, suggests that the electron-withdrawing effect of aluminum places the boron in a more oxidized state. Due to the surface sensitivity of XPS and the low yield

View Article Online
DOI: 10.1039/D5YA00314H

of photoelectron emission for boron, it remains unclear whether boron preferentially resides at the surface of the particles or is distributed throughout the particle, including within the near-surface region. Depth profiling methods that can confirm a surface-enriched boron phase are limited by the detection threshold for boron in these materials, and a further challenge is quantification while milling a pile of particles of varying sizes and shapes[74]. Therefore, while the B 1s signal confirms the presence of boron oxides, it cannot alone establish the formation of a boron-rich surface layer or coating. Nonetheless, the persistence of the B 1s peak in the co-doped samples indicates that Al and Nb do not hinder the incorporation of B. These results also further suggest that boron has been incorporated into the NMC lattice. Although the spatial distribution of B, particularly its possible enrichment at the surface, requires further analysis using more boron-sensitive techniques with improved spatial resolution.

When both boron and niobium migrate to the particle surface during the high-temperature synthesis, it is plausible that mixed surface phases or layered interphases form that consist of niobium and boron oxides. Potential compounds include lithium niobate ($LiNbO_3$), niobium pentoxide (Nb_2O_5), lithium borates (e.g., $LiBO_2$ or Li_3BO_3)[75], or even complex mixed-metal borates or niobium borates (such as $NbBO_4$ or Li–Nb–B–O amorphous phases), although the latter are more speculative due to limited thermodynamic data available in the literature. The coexistence of these species could result in a multifunctional surface layer that combines the benefits of both Nb- and B-containing compounds. Niobium oxides are known to be chemically stable and exhibit a wide electrochemical window, acting as physical barriers that suppress electrolyte decomposition and transition metal dissolution[76]. Boron-containing species, on the other hand, tend to form glassy, amorphous structures that can chemically buffer acidic electrolyte components and further inhibit surface reconstruction[77]. Suppose that both species segregate to the surface and interact

View Article Online
DOI: 10.1039/D5YA00314H

during the calcination process. In that case, they may form a chemically complex, composite interphase that is mechanically resilient and potentially lithium-conductive, depending on its degree of crystallinity and lithium content. Such a hybrid layer may enhance the cathode's surface stability, mitigate parasitic reactions, and preserve the layered structure of NMC by limiting oxygen loss and TM reduction. However, the exact structure and function of these mixed-phase coatings would depend heavily on the local stoichiometry, thermal processing conditions, and precursor decomposition pathways.

Electrochemical Evaluation of Multi-Element Doped NMC 811 Cathodes

The cycling stability and rate capability of pristine and modified NMC 811 cathodes were evaluated through galvanostatic cycling and rate capability tests. **Figure 7** illustrates the mean cycling performance of three half-cells each for pristine NMC 811 and the boron-, aluminum, and niobium-modified compositions at a constant charge/discharge rate (C-rate) of 1C (i.e., a rate corresponding to the battery achieving a full charge in 1 h). The B-NMC 811 exhibits the most pronounced capacity fade of this series of custom-prepared NMC 811 samples. Samples co-doped with boron along with aluminum and/or niobium retain higher capacities over extended periods of cycling. All cells were cycled at a rate of 1C for 100 cycles at 25 °C. The pristine NMC 811 (purple trace) exhibits a significant capacity fade, decreasing from 182 mAh/g to 138 mAh/g over 100 cycles, resulting in a capacity retention of 75.8%. This degradation is indicative of structural instability, which has been previously observed for NMC 811 cycled at 25 °C[78,79]. The B-NMC 811 sample (green trace) exhibits the worst capacity retention, decaying at a faster rate than the pristine NMC 811 and retaining only about 72.5% of its initial capacity of 169 mAh/g. Boron doping alone is insufficient to stabilize the structure. In fact, the presence of B as the only dopant may exacerbate the degradation mechanisms in this system by introducing lattice distortions. This

View Article Online
DOI: 10.1039/D5YA00314H

trend is distinct from some other observations in the literature for NMC 811 and is likely a function of the synthetic methods[50,51]. As mentioned earlier, the concentration of boron used in this study may also be too high for the synthetic method utilized herein, potentially causing a lithium deficiency, as boron can react with Li^+, and subsequently result in a larger degree of cation mixing as it gives Ni^{2+} an opportunity to fill Li^+ vacancies, which directly impedes Li^+ diffusion and severely limits both the initial specific capacity and rate capability. The introduction of aluminum and/or niobium stabilizes the B-NMC structure, as evidenced by the enhanced cycling retention of these co-doped samples. The best overall performance is observed for B-Al-Nb-NMC 811 (black trace), which decreases from 185 mAh/g to 167 mAh/g over the 100 cycles, corresponding to a capacity retention of ~90.5% (**Table 2**). The B-Nb-NMC 811 sample also exhibits a similar overall performance to the B-Al-Nb-NMC 811 sample. Niobium can form a thin coating on the NMC 811 particles (**Figure 3a and 3c**), protecting the cathode from electrolyte contact. In addition, niobium exhibits synergistic effects when incorporated with aluminum to stabilize the layered NMC 811 structure, reducing phase transitions and minimizing cation disorder. The results suggest that applying a coating, in addition to co-doping, can effectively mitigate phase instability and suppress detrimental cation migration, leading to prolonged electrochemical stability for NMC 811 cathode materials.

A comparison of the mean rate capabilities of this series of custom NMC 811 cathodes demonstrates that multi-element doping with boron, aluminum, and niobium delivers the highest and most stable specific discharge capacity across all C-rates compared to other doped and pristine NMC 811 samples (**Figure 8**). At low current densities, such as 0.1C and 0.5C, most of the samples display a similar capacity around 200 mAh/g, indicating a comparable initial performance. The B-NMC was the anomaly with a much lower initial specific discharge capacity. With the increase in

View Article Online
DOI: 10.1039/D5YA00314H

C-rate, the pristine NMC 811 and B-NMC 811 exhibit significant capacity fading, with B-NMC 811 showing the steepest decline, especially at higher rates, such as 5C and 10C. In contrast, the co-doped samples, particularly B-Al-NMC 811, B-Nb-NMC 811, and B-Al-Nb-NMC 811, maintained higher capacities and exhibited less degradation, suggesting improved structural stability and enhanced lithium-ion transport kinetics. Upon returning to 0.1C at the end of the test, the co-doped samples more effectively recovered their capacities than the pristine NMC 811, further indicating their superior rate capability and reversibility.

To investigate the impact of boron, aluminum, and niobium doping on the reversibility of cycling the NMC 811, a differential capacity (dQ/dV) analysis was performed throughout the course of 100 cycles. The dQ/dV plots (**Figure 9**) provide insights into each material's phase transitions during the charge and discharge processes by tracking the evolution of the observed redox peaks during lithium intercalation and deintercalation. A decrease in peak intensity, a shift in peak position, and peak broadening can indicate structural degradation, cation mixing, and increasing polarization during the cycling process. The pristine NMC 811 exhibits a series of well-defined oxidation and reduction peaks in the first cycle, consistent with the characteristic phase transitions of layered NMC materials[80]. However, as cycling progresses to the 50th and 100th cycle, the peaks undergo a significant reduction in their intensity and peak broadening. This degradation suggests an increasing irreversible polarization and a loss of structural integrity, likely due to cation mixing, microcrack formation, and electrolyte side reactions at the electrode surfaces[81]. These factors contribute to capacity fading, and the results are consistent with the observed capacity fade of the pristine NMC material in **Figure 7**. A similar trend is observed in the B-doped NMC 811, where peak broadening and fading occur at a comparable rate to the pristine material. There is a significant decrease in intensity and an increase in peak voltage for the H2→H3 phase

View Article Online
DOI: 10.1039/D5YA00314H

transition between the 1st cycle and the 50th cycle, with this trend continuing upon reaching the 100th cycle. This coincides with the previously observed poor capacity retention of the B-NMC 811 material as prepared by the one-pot process used herein. Similar studies have shown that B-doped high-nickel NMC using H_3BO_3 as the boron precursor exhibited a similar trend, likely due to the irreversible H2→H3 phase transition[82].

In contrast, the B-Al-NMC 811, B-Nb-NMC 811, and B-Al-Nb-NMC 811 samples demonstrate a markedly improved stability. While some peak broadening and intensity loss are still evident after 100 cycles, the degradation is far less pronounced than in the pristine and B-NMC 811 materials. Notably, the voltages for H1→M and H3→H2 phase transitions remain stable, showing minimal shift in voltage from the 1st to 100th cycle. The peaks associated with the more detrimental H2→H3 phase transition also retain significantly more of their initial intensity and exhibit less voltage shift compared to the changes observed in the pristine and B-NMC 811 samples. This suggests that the synergistic co-doping of boron with aluminum and niobium effectively suppresses the detrimental phase transitions at high voltages. By stabilizing the crystal structure, the dopants mitigate the primary degradation mechanisms, leading to the superior capacity retention and cycling stability observed in **Figure 7**.

Conclusions

This study demonstrates the effectiveness of a multi-element doping and coating strategy in stabilizing high-nickel NMC 811 cathode materials. Through the one-pot M2CAM® synthesis approach, we successfully introduce boron, aluminum, and niobium simultaneously into the NMC 811 structure, both within the bulk lattice and on the particle surface. The co-modified B-Al-Nb-NMC 811 material exhibited superior electrochemical performance, with a capacity retention of ~91% after 100 cycles at 1C, significantly outperforming the pristine and singly doped

View Article Online
DOI: 10.1039/D5YA00314H

counterparts. Structural and surface analysis revealed that while boron doping alone introduced unfavorable morphological changes, such as the formation of smaller, blockier primary particles, and structural degradation as evidenced by a significant increase in cation mixing, the synergistic incorporation of aluminum and niobium mitigated these effects. Aluminum stabilized the crystal structure internally, while niobium contributed to the formation of a thin, surface-enriched coating, as confirmed by STEM-EDS and XPS, that reduced electrolyte-induced degradation. XRD analyses confirmed reduced cation mixing relative to the pristine and boron-only doped material, while XPS confirmed the presence of surface-localized Nb species, supporting the proposed mechanisms for stabilization of the NMC lattice during cycling. Together, these findings confirm that the combination of boron, aluminum, and niobium enhances both bulk and interfacial stability, offering a promising route to extend the cycle life and rate performance of nickel-rich cathode materials for next-generation lithium-ion batteries. Future studies should, however, focus on pinpointing the exact locations of the B species within the lattice and on the surface of the NMC 811 particles with respect to other dopants. These analyses will require advanced characterization techniques, such as Meitner-Auger electron spectroscopy, which can provide the necessary spatial resolution and elemental sensitivity at the low concentrations of dopant used herein. Additionally, comprehensive electrochemical impedance spectroscopy (EIS) investigations are planned for future studies to quantitatively assess differences in the evolution of charge transfer resistances between each sample type and to further elucidate the role of these multi-element surface coatings during extended cycling.

View Article Online
DOI: 10.1039/D5YA00314H

CRediT

Rex Chen – Conceptualization; Data curation; Formal analysis; Investigation; Methodology; Project administration; Visualization; Writing – Original draft; Writing – Review & editing

Vahid Moradi – Resources; Visualization; Formal analysis; Writing – Review & editing

Lida Hadidi – Conceptualization; Funding acquisition; Formal analysis; Writing – Review & editing

Byron D. Gates – Conceptualization; Formal analysis; Resources; Funding acquisition; Methodology; Project Administration; Supervision; Writing – Review & editing

Conflict of Interest

The authors confirm no competing financial interest.

Data Availability

The data supporting this article are included in the supplementary information (SI). Data include particle size analysis plots and tabulated results, XRD including Rietveld refinements, EDS-based elemental maps and spectra, survey and high-resolution XPS data, and ICP-OES of the pristine and co-doped/coated NMC 811 particles before and after thermal processing, theoretical weights and atomic percentages of dopants, and discharge capacity of all samples during the pre-cycling conditioning. See DOI: https://doi.org/xxx

Acknowledgements

This research was conducted in collaboration with Nano One Materials Corp. supported in part by MITACS (Reference No. R832743), the Natural Sciences and Engineering Research

View Article Online
DOI: 10.1039/D5YA00314H

Council of Canada (NSERC; Grant No. RGPIN-2020-06522), and a Simon Fraser University Graduate Fellowship (R. Chen). This work used 4D LABS at Simon Fraser University (SFU) and the Center for Soft Materials shared facilities, supported by the Canada Foundation for Innovation (CFI), British Columbia Knowledge Development Fund (BCKDF), Western Economic Diversification Canada, and SFU. This work also utilized the nanoFAB at the University of Alberta to obtain the XPS measurements.

View Article Online
DOI: 10.1039/D5YA00314H

Tables

Table 1. Calculated lattice parameters of pristine and modified NMC 811 materials.

material	a (Å)	c (Å)	c/a	lattice volume (Å^3)	measured I_{003}/I_{104}	Rwp* (%)
pristine NMC 811	2.8711(3)	14.1944(2)	4.9440	101.328	1.4326	5.24
B-NMC 811	2.8726(5)	14.1819(4)	4.9370	101.346	0.9911	5.27
B-Al-NMC 811	2.8710(4)	14.1849(3)	4.9408	101.256	1.0809	5.51
B-Nb-NMC 811	2.8729(5)	14.1970(3)	4.9418	101.474	1.2829	5.30
B-Al-Nb-NMC 811	2.8734(9)	14.1937(5)	4.9397	101.488	1.0992	5.38

abbreviations: *Rwp = weighted profile residual

Table 2. Capacity retention of the pristine and custom-modified NMC 811 cathode materials.

material	capacity retention (%)
pristine NMC 811	75.8
B-NMC 811	72.5
B-Al-NMC 811	86.5
B-Nb-NMC 811	90.9
B-Al-Nb-NMC 811	90.5

View Article Online
DOI: 10.1039/D5YA00314H

Figures

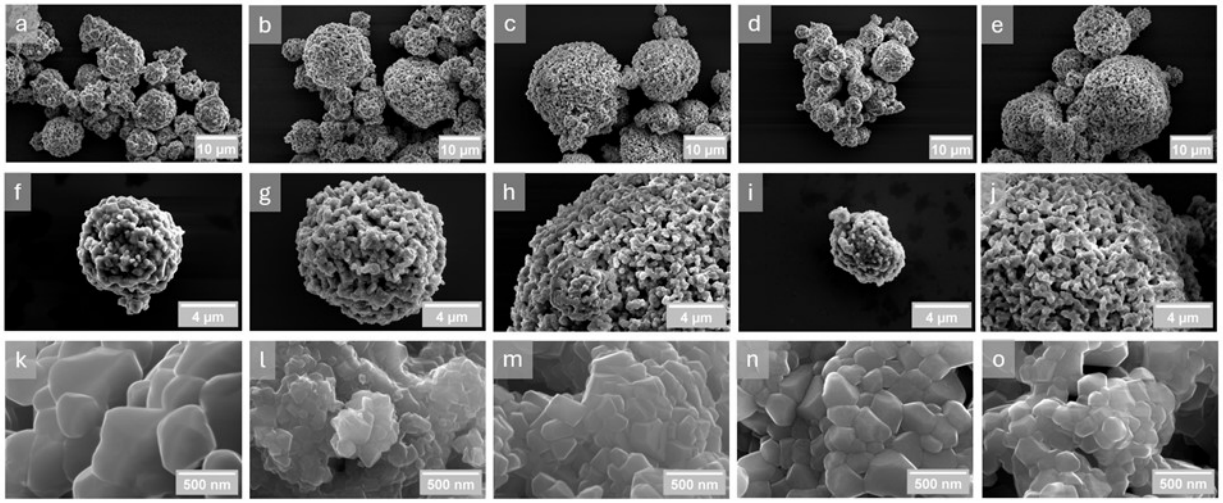

Figure 1. Scanning electron microscopy (SEM) images of (a, f, k) pristine NMC 811 and NMC doped with boron, as well as co-doping with aluminum and/or niobium: (b, g, l) B-NMC 811; (c, h, m) B-Al-NMC 811, (d, i, n) B-Nb-NMC 811, and (e, j, o) B-Al-Nb-NMC 811 particles at different magnifications.

View Article Online
DOI: 10.1039/D5YA00314H

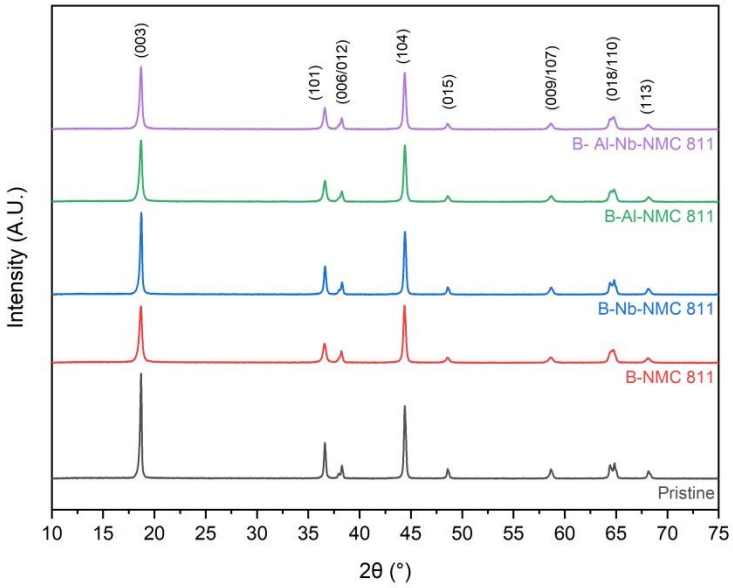

Figure 2. X-ray diffraction (XRD) patterns of pristine NMC 811 and B-doped, B-Nb-doped, B-Al-doped, and B-Al-Nb-doped NMC 811. Peaks are indexed to the $R\bar{3}m$ space group, which confirms the formation of a layered structure.

View Article Online
DOI: 10.1039/D5YA00314H

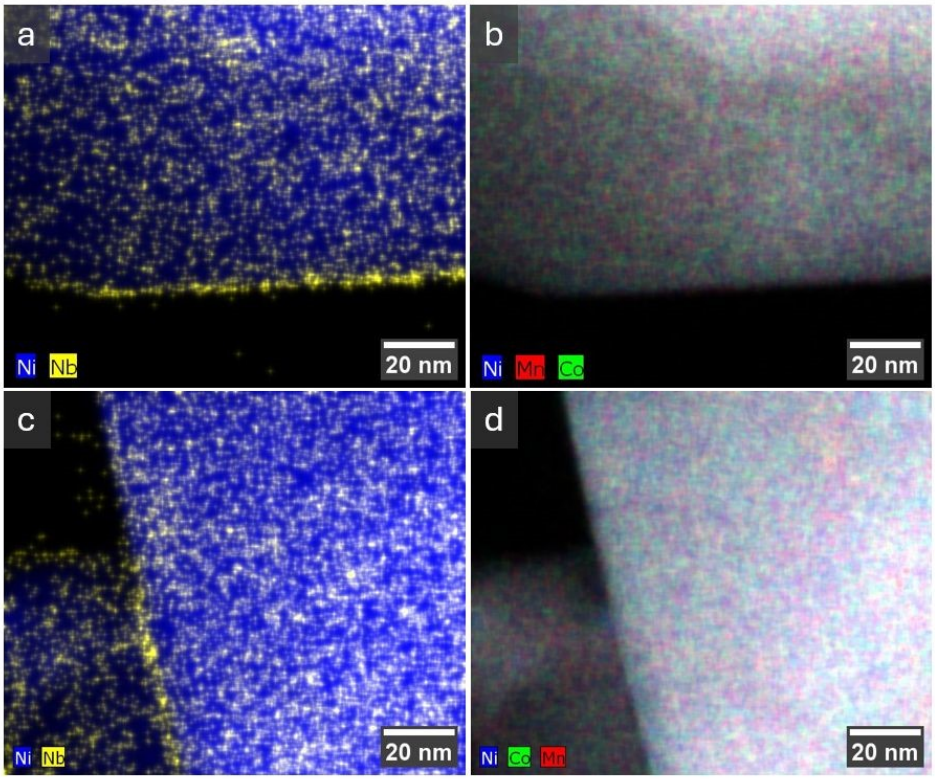

Figure 3. Representative images obtained by scanning transmission electron microscopy (STEM) with overlaid elemental maps from energy dispersive X-ray spectroscopy (EDS) of the surfaces of the (a) B-Nb-NMC 811 and (c) B-Al-Nb-NMC 811 particles. Combined STEM and EDS data depicting the distributions of transition metals in the (b) B-Nb-NMC 811 and (d) B-Al-Nb-NMC 811 samples.

View Article Online
DOI: 10.1039/D5YA00314H

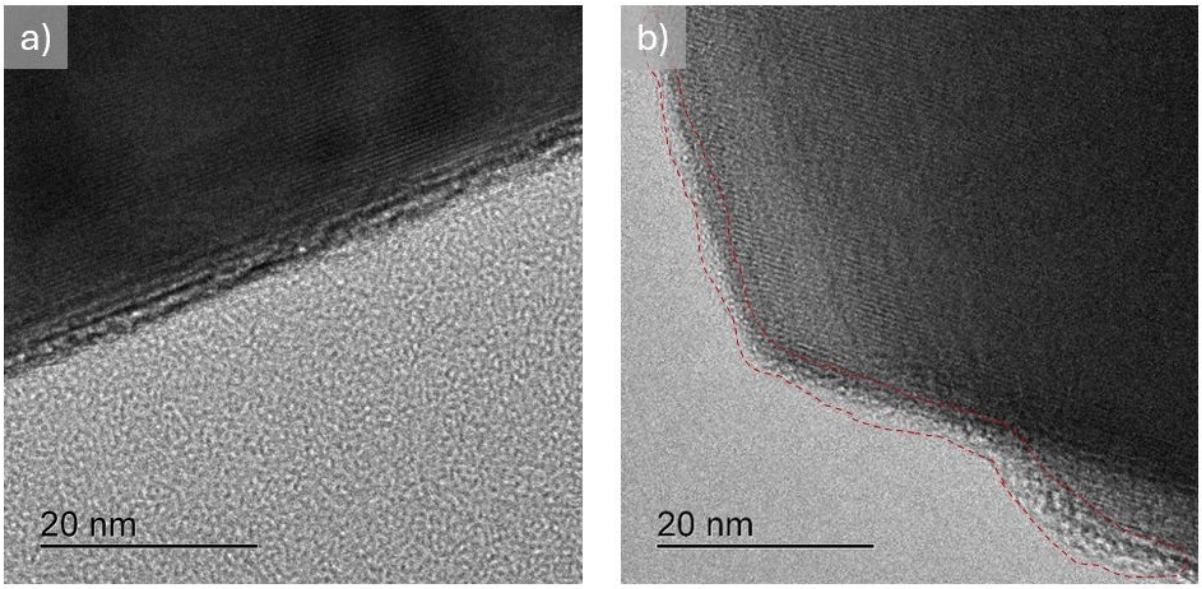

Figure 4. High-resolution transmission electron microscopy (HRTEM) images of primary particle surfaces for (a) pristine NMC 811 and (b) B-Nb-NMC 811. A distinct amorphous surface coating in (b) is delineated by red dashed lines.

View Article Online
DOI: 10.1039/D5YA00314H

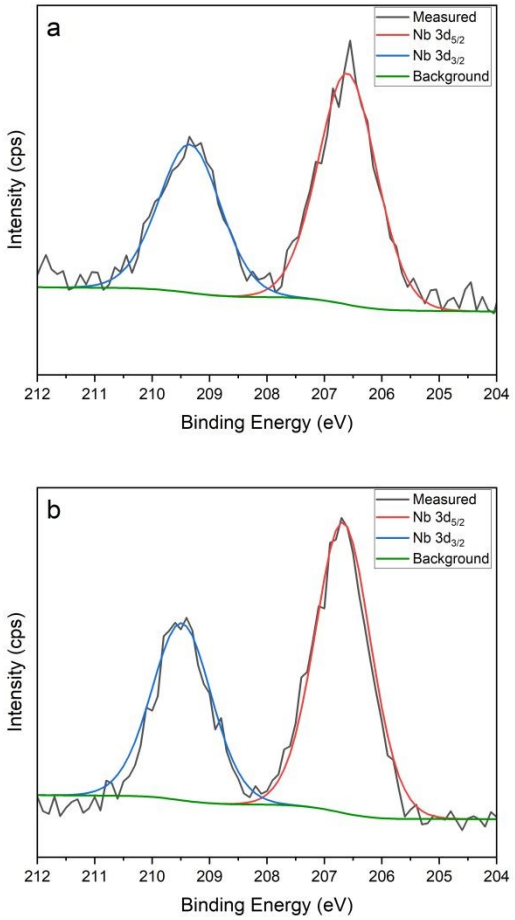

Figure 5. The high-resolution X-ray photoelectron spectroscopy (XPS) results for Nb 3d in (a) B-Nb-NMC 811 and (b) B-Al-Nb-NMC 811 cathode particles.

View Article Online
DOI: 10.1039/D5YA00314H

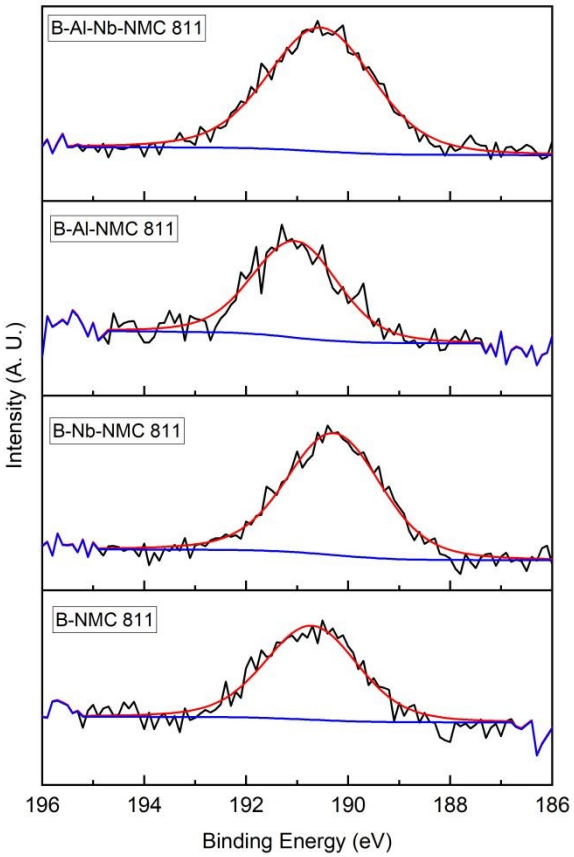

Figure 6. High-resolution B1s XPS results (from bottom to top trace) for (i) B-NMC 811, (ii) B-Nb-NMC 811, (iii) B-Al-NMC 811, and (iv) B-Al-Nb-NMC 811 particles.

View Article Online
DOI: 10.1039/D5YA00314H

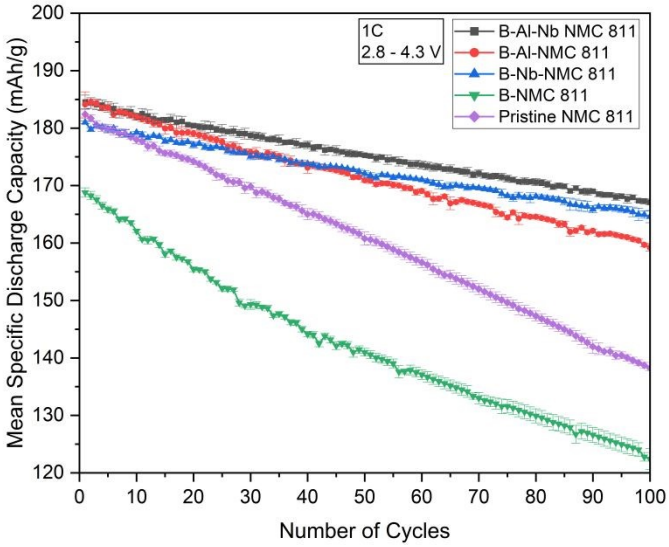

Figure 7. Mean specific discharge capacities obtained at 1C, cycling between 2.8 and 4.3 V (vs Li/Li^+), for the pristine NMC 811 and the series of modified NMC 811 materials, as indicated in the legend.

View Article Online
DOI: 10.1039/D5YA00314H

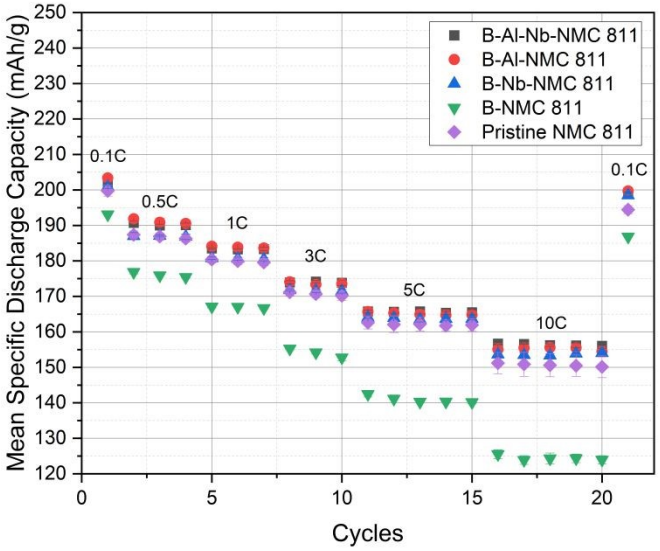

Figure 8. Mean rate capabilities of pristine and custom-modified NMC 811 materials as a function of different C-rates, as indicated on the plot.

View Article Online
DOI: 10.1039/D5YA00314H

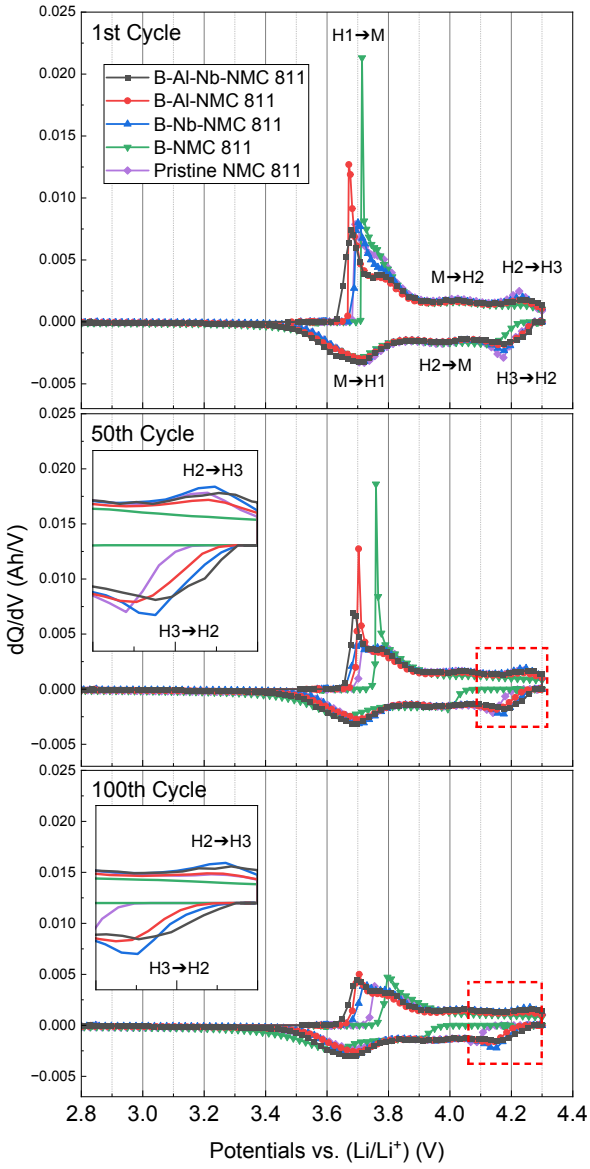

Figure 9. Differential capacity curves of the (i) pristine NMC 811, (ii) B-NMC 811, (iii) B-Nb-NMC 811, (iv) B-Al-NMC 811, (v) B-Al-Nb-NMC 811 samples at the 1st cycle (top plot), 50th cycle (middle plot), and 100th cycle (bottom plot). Inset images show magnified views of the regions outlined by the boxes with red dashed lines.

View Article Online
DOI: 10.1039/D5YA00314H

References

1. E. D. Orlova, A. A. Savina, S. A. Abakumov, A. V. Morozov and A. M. Abakumov, *Symmetry*, 2021, **13**, 1628.
2. Z. Yang, J. Zhang, M. C. W. Kintner-Meyer, X. Lu, D. Choi, J. P. Lemmon and J. Liu, *Chem. Rev.*, 2011, **111**, 3577–3613.
3. N. Nitta, F. Wu, J. T. Lee and G. Yushin, *Mater. Today*, 2015, **18**, 252–264.
4. M. Li, J. Lu, Z. Chen and K. Amine, *Adv. Mater.*, 2018, **30**, 1800561.
5. D. Deng, *Energy Sci. Eng.*, 2015, **3**, 385–418.
6. A. Manthiram, *ACS Cent. Sci.*, 2017, **3**, 1063–1069.
7. E. McCalla, A. W. Rowe, R. Shunmugasundaram and J. R. Dahn, *Chem. Mater.*, 2013, **25**, 989–999.
8. M. Li and J. Lu, *Science*, 2020, **367**, 979–980.
9. B. K. Sovacool, *Extr. Ind. Soc.*, 2019, **6**, 915–939.
10. J. Xu, F. Lin, M. M. Doeff and W. Tong, *J. Mater. Chem. A*, 2017, **5**, 874–901.
11. H.-J. Noh, S. Youn, C. S. Yoon and Y.-K. Sun, *J. Power Sources*, 2013, **233**, 121–130.
12. B. Xu, D. Qian, Z. Wang and Y. S. Meng, *Mater. Sci. Eng. R Rep.*, 2012, **73**, 51–65.
13. W. Li, B. Song and A. Manthiram, *Chem Soc Rev*, 2017, **46**, 3006–3059.
14. J. H. Yang, H. Kim and G. Ceder, *Molecules*, 2021, **26**, 3173.
15. S.-K. Jung, H. Gwon, J. Hong, K.-Y. Park, D.-H. Seo, H. Kim, J. Hyun, W. Yang and K. Kang, *Adv. Energy Mater.*, 2014, **4**, 1300787.
16. N. Iqbal, J. Choi, C. Lee, H. M. U. Ayub, J. Kim, M. Kim, Y. Kim, D. Moon and S. Lee, *Mathematics*, 2022, **10**, 4697.

View Article Online
DOI: 10.1039/D5YA00314H

17. J. C. Stallard, L. Wheatcroft, S. G. Booth, R. Boston, S. A. Corr, M. F. L. De Volder, B. J. Inkson and N. A. Fleck, *Joule*, 2022, **6**, 984–1007.

18. Y. Chen, W. Zhao, Q. Zhang, G. Yang, J. Zheng, W. Tang, Q. Xu, C. Lai, J. Yang and C. Peng, *Adv. Funct. Mater.*, 2020, **30**, 2000396.

19. R. Jung, M. Metzger, F. Maglia, C. Stinner and H. A. Gasteiger, *J. Electrochem. Soc.*, 2017, **164**, A1361.

20. Z. Ahaliabadeh, X. Kong, E. Fedorovskaya and T. Kallio, *J. Power Sources*, 2022, **540**, 231633.

21. F. Xin, H. Zhou, X. Chen, M. Zuba, N. Chernova, G. Zhou and M. S. Whittingham, *ACS Appl. Mater. Interfaces*, 2019, **11**, 34889–34894.

22. P. Kumari and R. Kundu, *Energy Fuels*, 2025, **39**, 10933–10966.

23. M. Eilers-Rethwisch, M. Winter and F. M. Schappacher, *J. Power Sources*, 2018, **387**, 101–107.

24. E. G. Lee, H. Park, S. Ji, S. J. Seong, M. Wu, S. S. Lee, Y. Kim and S. Choi, *Inorg. Chem.*, 2021, **60**, 16294–16302.

25. Y. Gao, J. Park and X. Liang, *ACS Appl. Energy Mater.*, 2020, **3**, 8978–8987.

26. S. Sharifi-Asl, J. Lu, K. Amine and R. Shahbazian-Yassar, *Adv. Energy Mater.*, 2019, **9**, 1900551.

27. S.-B. Lee, N.-Y. Park, G.-T. Park, U.-H. Kim, S.-J. Sohn, M.-S. Kang, R. M. Ribas, R. S. Monteiro and Y.-K. Sun, *ACS Energy Lett.*, 2024, **9**, 740–747.

28. L. Yin, Z. Li, G. S. Mattei, J. Zheng, W. Zhao, F. Omenya, C. Fang, W. Li, J. Li, Q. Xie, E. M. Erickson, J.-G. Zhang, M. S. Whittingham, Y. S. Meng, A. Manthiram and P. G. Khalifah, *Chem. Mater.*, 2020, **32**, 1002–1010.

View Article Online
DOI: 10.1039/D5YA00314H

29. G. Kaur and B. D. Gates, *J. Electrochem. Soc.*, 2022, **169**, 043504.

30. L. Shaw and M. Ashuri, *Adv. Mater. Lett.*, 2019, **10**, 369–380.

31. B. Xiao and X. Sun, *Adv. Energy Mater.*, 2018, **8**, 1802057.

32. U. Nisar, R. Petla, S. A. Jassim Al-Hail, A. A. Quddus, H. Monawwar, A. Shakoor, R. Essehli and R. Amin, *RSC Adv*, 2020, **10**, 15274–15281.

33. M. J. Herzog, D. Esken and J. Janek, *Batter. Supercaps*, 2021, **4**, 1003–1017.

34. M. Bandpey, M. Dorri, A. Babaei, C. Zamani and M. Bortolotti, *ACS Appl. Energy Mater.*, 2023, **6**, 7974–7984.

35. M. J. Herzog, N. Gauquelin, D. Esken, J. Verbeeck and J. Janek, *ACS Appl. Energy Mater.*, 2021, **4**, 8832–8848.

36. F. Nagler, N. Christian, A. Gronbach, F. Stahl, P. Daubinger, A. Flegler, M. Hofmann and G. A. Giffin, *ChemElectroChem*, 2024, **11**, e202300748.

37. K. Wang, Q. Mao, X. Lu, J. Zhang, H. Huang, Y. Gan, X. He, X. Xia, W. Zhang and Y. Xia, *Sustain. Mater. Technol.*, 2023, **38**, e00713.

38. K. V. Nefedova, V. D. Zhuravlev, A. M. Murzakaev, V. V. Yagodin, M. V. Kuznetsov, E. Yu. Evshchik, V. M. Skachkov and O. V. Bushkova, *Russ. J. Electrochem.*, 2021, **57**, 1055–1069.

39. U. Nisar, J. Bansmann, M. Hebel, B. Reichel, M. Mancini, M. Wohlfahrt-Mehrens, M. Hölzle and P. Axmann, *Chem. Eng. J.*, 2024, **493**, 152416.

40. N. R. Park, Y. Li, W. Yao, M. Zhang, B. Han, C. Mejia, B. Sayahpour, R. Shimizu, B. Bhamwala, B. Dang, S. Kumakura, W. Li and Y. S. Meng, *Adv. Funct. Mater.*, 2024, **34**, 2312091.

41. Z. Chen, Y. Qin, K. Amine and Y.-K. Sun, *J Mater Chem*, 2010, **20**, 7606–7612.

View Article Online
DOI: 10.1039/D5YA00314H

42. M. Aykol, S. Kirklin and C. Wolverton, *Adv. Energy Mater.*, 2014, **4**, 1400690.

43. Z. Ahaliabadeh, V. Miikkulainen, M. Mäntymäki, S. Mousavihashemi, J. Lahtinen, Y. Lide, H. Jiang, K. Mizohata, T. Kankaanpää and T. Kallio, *ACS Appl. Mater. Interfaces*, 2021, **13**, 42773–42790.

44. J. Park and T. Yim, *Appl. Surf. Sci.*, 2024, **663**, 160195.

45. M. Lee, W. Ahmad, D. W. Kim, K. M. Kwon, H. Y. Kwon, H.-B. Jang, S.-W. Noh, D.-H. Kim, S. J. A. Zaidi, H. Park, H. C. Lee, M. Abdul Basit and T. J. Park, *Chem. Mater.*, 2022, **34**, 3539–3587.

46. S. Engün, K. B. Dermenci, U. Savacı, C. C. Erdoğan and S. Turan, *J. Alloys Compd.*, 2023, **957**, 170466.

47. M. Al-Shroofy, Q. Zhang, J. Xu, T. Chen, A. P. Kaur and Y.-T. Cheng, *J. Power Sources*, 2017, **352**, 187–193.

48. C. Henriksen, J. K. Mathiesen and D. B. Ravnsbæk, *Solid State Ion.*, 2020, **344**, 115152.

49. K.-J. Park, H.-G. Jung, L.-Y. Kuo, P. Kaghazchi, C. S. Yoon and Y.-K. Sun, *Adv. Energy Mater.*, 2018, **8**, 1801202.

50. C.-Y. Wu, Q. Bao, Y.-T. Tsai and J.-G. Duh, *J. Alloys Compd.*, 2021, **865**, 158806.

51. Y. Liu, X. Fan, B. Luo, Z. Zhao, J. Shen, Z. Liu, Z. Xiao, B. Zhang, J. Zhang, L. Ming and X. Ou, *J. Colloid Interface Sci.*, 2021, **604**, 776–784.

52. F. Xin, H. Zhou, Y. Zong, M. Zuba, Y. Chen, N. A. Chernova, J. Bai, B. Pei, A. Goel, J. Rana, F. Wang, K. An, L. F. J. Piper, G. Zhou and M. S. Whittingham, *ACS Energy Lett.*, 2021, **6**, 1377–1382.

53. J. Li, W. Li, S. Wang, K. Jarvis, J. Yang and A. Manthiram, *Chem. Mater.*, 2018, **30**, 3101–3109.

View Article Online
DOI: 10.1039/D5YA00314H

54. S. A. Campbell, US Pat., 20210359300A1, 2021.

55. S.A. Campbell, T. E. Rowe, US Pat., 20220064019A1, 2022.

56. A. Manthiram, B. Song and W. Li, *Energy Storage Mater.*, 2017, **6**, 125–139.

57. S. Aryal, J. L. Durham, A. L. Lipson, K. Z. Pupek and O. Kahvecioglu, *Electrochimica Acta*, 2021, **391**, 138929.

58. A. C. Wagner, N. Bohn, H. Geßwein, M. Neumann, M. Osenberg, A. Hilger, I. Manke, V. Schmidt and J. R. Binder, *ACS Appl. Energy Mater.*, 2020, **3**, 12565–12574.

59. C. Roitzheim, L.-Y. Kuo, Y. J. Sohn, M. Finsterbusch, S. Möller, D. Sebold, H. Valencia, M. Meledina, J. Mayer, U. Breuer, P. Kaghazchi, O. Guillon and D. Fattakhova-Rohlfing, *ACS Appl. Energy Mater.*, 2022, **5**, 524–538.

60. T. M. M. Heenan, A. Wade, C. Tan, J. E. Parker, D. Matras, A. S. Leach, J. B. Robinson, A. Llewellyn, A. Dimitrijevic, R. Jervis, P. D. Quinn, D. J. L. Brett and P. R. Shearing, *Adv. Energy Mater.*, 2020, **10**, 2002655.

61. S. S. Shishvan, N. A. Fleck, R. M. McMeeking and V. S. Deshpande, *J. Power Sources*, 2023, **588**, 233745.

62. F. Xin, A. Goel, X. Chen, H. Zhou, J. Bai, S. Liu, F. Wang, G. Zhou and M. S. Whittingham, *Chem. Mater.*, 2022, **34**, 7858–7866.

63. F. Xin, H. Zhou, J. Bai, F. Wang and M. S. Whittingham, *J. Phys. Chem. Lett.*, 2021, **12**, 7908–7913.

64. X. Zhang, W. J. Jiang, A. Mauger, Qilu, F. Gendron and C. M. Julien, *J. Power Sources*, 2010, **195**, 1292–1301.

65. T. E. Ashton, P. J. Baker, C. Sotelo-Vazquez, C. J. M. Footer, Kenji. M. Kojima, T. Matsukawa, T. Kamiyama and J. A. Darr, *J Mater Chem A*, 2021, **9**, 10477–10486.

View Article Online
DOI: 10.1039/D5YA00314H

66. M. Bianchini, M. Roca-Ayats, P. Hartmann, T. Brezesinski and J. Janek, *Angew. Chem. Int. Ed.*, 2019, **58**, 10434–10458.

67. L. R. Sheppard, *J. Phys. Chem. C*, 2013, **117**, 3407–3413.

68. L. R. Sheppard, A. J. Atanacio, T. Bak, J. Nowotny, M. K. Nowotny and K. E. Prince, *J. Solid State Electrochem.*, 2009, **13**, 1115–1121.

69. N. Li, X. Lan, L. Wang, Y. Jiang, S. Guo, Y. Li and X. Hu, *ACS Appl. Mater. Interfaces*, 2021, **13**, 16445–16453.

70. K. Doyle-Davis, K. Adair, C. Wang, F. Zhao, S. Deng and X. Sun, *Battery Energy*, 2024, **3**, 20230051.

71. L. Yao, H. Zheng, H. Yu, L. Chen and H. Jiang, *Energy Fuels*, 2023, **37**, 16962–16969.

72. W. Mo, Z. Wang, J. Wang, X. Li, H. Guo, W. Peng and G. Yan, *Chem. Eng. J.*, 2020, **400**, 125820.

73. S. Oswald and H. Wirth, *Surf. Interface Anal.*, 1999, **27**, 136–141.

74. H. Shimada, K. Sato, N. Matsubayashi, M. Imamura, T. Saito and K. Furuya, *Appl. Surf. Sci.*, 1999, **144–145**, 21–25.

75. P. Kumari and R. Kundu, *Energy Fuels*, 2025, **39**, 10933–10966.

76. G. Gabrielli, P. Axmann, T. Diemant, R. J. Behm and M. Wohlfahrt-Mehrens, *ChemSusChem*, 2016, **9**, 1670–1679.

77. J. Dou, X. Kang, T. Wumaier, H. Yu, N. Hua, Y. Han and G. Xu, *J. Solid State Electrochem.*, 2012, **16**, 1481–1486.

78. M. Wood, J. Li, R. E. Ruther, Z. Du, E. C. Self, H. M. Meyer, C. Daniel, I. Belharouak and D. L. Wood, *Energy Storage Mater.*, 2020, **24**, 188–197.

View Article Online
DOI: 10.1039/D5YA00314H

79. G. J. Páez Fajardo, M. Belekoukia, S. Bolloju, E. Fiamegkou, A. S. Menon, Z. Ruff, Z. Shen, N. Shah, E. Björklund, M. J. Zuba, T.-L. Lee, P. K. Thakur, R. S. Weatherup, A. Aguadero, M. J. Loveridge, C. P. Grey and L. F. J. Piper, *RSC Appl Interfaces*, 2024, **1**, 133–146.

80. P. J. West, C. D. Quilty, Z. Wang, S. N. Ehrlich, L. Ma, C. Jaye, D. A. Fischer, X. Tong, A. M. Kiss, E. S. Takeuchi, A. C. Marschilok, K. J. Takeuchi and D. C. Bock, *J. Phys. Chem. C*, 2023, **127**, 7054–7070.

81. C. Busà, M. Belekoukia and M. J. Loveridge, *Electrochimica Acta*, 2021, **366**, 137358.

82. E. Williams, D. Burnett, P. Slater and E. Kendrick, *ChemElectroChem*, 2025, **12**, e202400677.

View Article Online
DOI: 10.1039/D5YA00314H

The data supporting this article are included in the supplementary information (SI). Data include particle size analysis plots and tabulated results, XRD including Rietveld refinements, EDS-based elemental maps and spectra, survey and high-resolution XPS data, and ICP-OES of the pristine and co-doped/coated NMC 811 particles before and after thermal processing, theoretical weights and atomic percentages of dopants, and discharge capacity of all samples during the pre-cycling conditioning. See DOI: https://doi.org/xxx